

USING CONVOLUTIONAL NEURAL NETWORKS FOR RELATIVE POSE ESTIMATION OF A NON-COOPERATIVE SPACECRAFT WITH THERMAL INFRARED IMAGERY

Maxwell Hogan⁽¹⁾, Duarte Rondao⁽¹⁾, Nabil Aouf⁽¹⁾, and Olivier Dubois-Matra⁽²⁾

⁽¹⁾*City, University of London, ECV1 0HB London, United Kingdom,
{firstname.lastname}@city.ac.uk*

⁽²⁾*European Space Agency, ESTEC, Keplerlaan 1, 2201 AZ Noordwijk, The Netherlands,
olivier.dubois-matra@esa.int*

ABSTRACT

Recent interest in on-orbit servicing and Active Debris Removal (ADR) missions have driven the need for technologies to enable non-cooperative rendezvous manoeuvres. Such manoeuvres put heavy burden on the perception capabilities of a chaser spacecraft. This paper demonstrates Convolutional Neural Networks (CNNs) capable of providing an initial coarse pose estimation of a target from a passive thermal infrared camera feed. Thermal cameras offer a promising alternative to visible cameras, which struggle in low light conditions and are susceptible to overexposure. Often, thermal information on the target is not available *a priori*; this paper therefore proposes using visible images to train networks. The robustness of the models is demonstrated on two different targets, first on synthetic data, and then in a laboratory environment for a realistic scenario that might be faced during an ADR mission. Given that there is much concern over the use of CNNs in critical applications due to their black box nature, we use innovative techniques to explain what is important to our network and fault conditions.

KEYWORDS

Deep Learning; Explainable Artificial Intelligence, Computer Vision; Spacecraft Pose Estimation; Active Debris Removal.

1 INTRODUCTION

Autonomous rendezvous and docking missions such as the International Space Station (ISS) resupply missions undertaken by the European Automated Transfer Vehicle (ATV) and more recently, SpaceX Cargo Dragon have had the advantage of a cooperating target. Markers and additional sensors on the target, and a physical interface to grapple, were used to ensure a safe rendezvous. However, recent interests have shifted to technologies for use in situations where the target is unresponsive such as Active Debris Removal (ADR) missions. The lack of aid from the target puts higher responsibility on the chaser's Guidance, Navigation, and Control (GNC) system. To the authors' knowledge, such a manoeuvre has only been achieved once with the capture of and relaunch of the IntelSat VI satellite which required human intervention for success [1].

A natural solution might be the use of a Light Detection and Ranging (LIDAR) system which has already seen use on the Space Shuttle. LIDAR sensors can supply range information with high accuracy without being susceptible to illumination changes which can be expected in on orbit conditions [2]. However, they remain difficult to install on small craft due to their size and heavy power requirements. On the other hand, passive sensors such as visible and infrared cameras are characterised by a lower hardware complexity and cheaper power consumption [2].

It is the motivation of this project to extend the capabilities of passive sensors for close-range relative navigation. Other works have presented the use of Convolutional Neural Networks (CNNs) to provide pose estimation of non-cooperative spacecraft on visible images; however, these works have proposed their use as a full-fledged coarse estimator [3, 4]. CNNs do not take into consideration the previous prediction and ignore the temporal relationship between predictions. This can result in high variance between the solutions of contiguous frames.

We have chosen to focus on a simpler problem statement which is to provide an initial estimation of the pose so that a more precise algorithm can make refinements. This had been previously achieved by Rondao *et al.* [5] where a Bayesian classifier, a traditional machine learning algorithm, was used to match 2D features from a visible camera feed to keyframes of the 3D target that were learned offline. This method does automatically extract feature from an image but these features must be determined by the developer beforehand. This presents a difficulty since a developer would have to consider the effect of a large possible scenarios when they are making their decision. Conversely, the features that are extracted by a CNNs are learned through optimisation. A CNNs can instead learn generalisations about the data that make it more stable for dealing with fringe cases.

Visible light cameras ($0.38\text{ }\mu\text{m}$ – $0.75\text{ }\mu\text{m}$) struggle to match the reliability of continuous measurements of active sensors due to the poor illumination conditions in eclipse and oversaturation from reflective surfaces or direct light from the sun. On the other hand, recent studies suggest that thermal infrared (or LWIR [Long Wavelength Infrared]) based cameras offer a promising alternative to vision-based or active technologies for non-cooperative rendezvous missions [6, 7]. According to a report by Yılmaz *et al.* [7], objects under direct illumination from the Sun should appear smoother in LWIR ($8\text{ }\mu\text{m}$ – $14\text{ }\mu\text{m}$) when compared to visible due to reflective surfaces such as thermal insulators. An additional benefit of LWIR images is the lack of shadows created by incident light; therefore, these should require less intensive pre-processing to clean the image.

A significant challenge in the development of LWIR-based CNNs is the lack of relevant thermal infrared datasets for training. Nevertheless, visible data of a target is often easily acquired and often already available. Therefore, it is the motivation of this study to investigate the robustness of a CNN tested on thermal images which has been trained exclusively on synthetic visible images. In the first phase of development, we focused primarily on synthetic data generated by the Astos camera simulator¹ and limited our pose estimate to a single degree of freedom. We trained two models based on Resnet18 [8] and Resnet34 on visible images of our considered target spacecraft, Envisat.

From our results on our synthetic images, we were able to demonstrate that Resnet-based architectures trained on visible images can be robust on LWIR images. We also found that the deeper networks were able to achieve higher F1 scores. Work by Hajebi and Zelek [6] has found that thermal infrared has its own unique challenges. These include noise and low resolution, reflections, halo effects or saturation, and history effects due to the time it takes temperature variations to propagate. These effects are difficult to model even when the thermal signature of the target is properly known. Hence, moving forward into the second stage of our phase of our development, we sought to demonstrate our model's robustness in going from synthetic to real imagery.

¹<https://www.astos.de/products/camsim>.

The aforementioned works on the use of CNNs for this application have failed to recognise they are complex and unintuitive tools, making them hard to trust in critical applications. This mistrust is based on the difficulty in understanding the origin source of failure cases and the consequent obstacles in debugging. This issue is not limited to our application: e.g., there is much concern over the use of Deep Neural Networks (DNNs) in general for Earth-bound autonomous vehicles [9]. In this study we investigate our network further to attempt to explain reasons for failure using Grad-CAM and better understand what it focuses on to make good predictions [10].

Grad-CAM allows us to explore which regions of the image, and thus which parts of the target, were most important to the model in making its decisions. Any image processing technique that utilises model-based pose estimation must consider the possibility that the non-cooperative target may be damaged, may contain movable sections, or that the model might contain incorrect dimensions or be missing features. Thus, the knowledge provided by Grad-CAM can assist in mission planning since we can consider whether a network's reliance on certain features may be inappropriate or not.

2 METHODOLOGY

2.1 Viewsphere Sampling

The objective of our algorithm is to provide an initial estimate of the relative orientation of the target based on its appearance. This information can then be passed to more precise pose estimation algorithms, or be used to cross-reference with another sensor reading, or algorithm prediction. In our study, we are not attempting to predict the roll angle of the camera, nor the position of the target relative to the chaser; instead, we are interested in recovering the viewpoint under which the target is being imaged by the chaser, modelled as a classification problem.

We utilise the same concept as Rondao *et al.* [5] of viewsphere sampling which is taken from 3D object detection. This concept imagines a sphere around the target, the surface of which is covered in cameras pointed toward the target at the centre, as can be seen in Fig. 1. Any viewpoint can be described using the spherical coordinates of a camera on this sphere.

During the first phase of our development we focused on one Degree-Of-Freedom (DOF), therefore the labels only corresponded to the azimuth. We used 10 classes, so that each class would represent a range of facets within 18 degrees from the centre of that class. The images in this dataset depicted the target spacecraft in a continuous roll, therefore there is variance in the observed facet within the classes.

During the second phase, we wanted to extend the pose estimation to two DOFs. Hence, each image was given two labels, one for the azimuth, and one for the elevation. We generated images for discrete steps of 10 degrees which were at the centre of our classes, therefore there is no variance in the observed facet within the class. Our new class scheme meant that each class represented a range of facets with 5 degrees from the centre of the class.

2.2 Network Architecture

CNNs are specifically suited for multidimensional data such as images [11]. They work on optimising convolutional kernels that are used to extract features from images. Deeper networks with more layers can extract more complicated features. However, deeper networks are also more prone to overfitting, something which can be problematic for our application since our test set is a different modality to

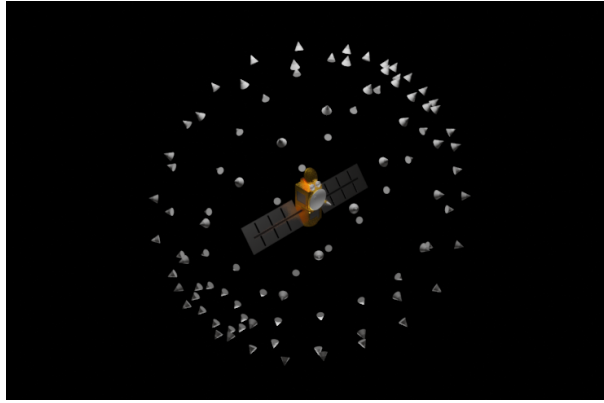


Fig. 1: Illustration of a viewsphere around our target spacecraft, Jason-1 (not to scale).

our training set. We want our network to be good at generalising the shapes of the object since the textures and shades will appear different between the visible and thermal modalities.

In order to overcome overfitting, the CNNs used in this study are adapted versions of ResNet. This network has demonstrated good generalisation from winning many competitions in image recognition and classifications [8]. It uses skip connections between layers in order to avoid the issue of vanishing gradients which occurs when training networks using gradient descent algorithms. In order to assist in training, ResNet utilises batch normalisation right after a convolution layer, and before an activation layer, this helps the gradient stay consistent, and not get so large that they slow down the network, or prevent it from training.

Unlike visible images, thermal images only have one colour channel that represents the heat radiance. Therefore, the first layer of the model was adapted to accept an image with a depth of 1. In our implementation we use a focus module, which was inspired from the first layer of YoloV5 [12]. The focus module transfers spatial information to the channel dimension, allowing us to use higher resolution input images without needing to adapt any other layers of the network, or increase the depth of the network. The benefit of a higher resolution image is that the features of the target are maintained, an important benefit when running inference on LWIR images which are typically lower resolution than visible images.

The final layer of the CNNs was adapted to suit our labels; in the first phase we adapted the number of outputs to 10, one for each class. This was changed again in the second phase when we shifted to predicting to two degrees of freedom. A single fully connected layer to predict would significantly reduce the number of samples available per class, whilst unnecessarily increasing the complexity of the model with a single layer with 648 possible classes. Therefore, two linear layers were added in parallel, one for each degree of freedom, one with 36 outputs for azimuth and the other with 18 for elevation.

2.3 Envisat Dataset

During the first phase of our development, we used a synthetic dataset generated by the Astos camera simulator featuring Envisat, a decommissioned oceanography satellite. Envisat was launched in 2002 and operated for over ten years until its mission was concluded in 2012 when communication was lost; it is currently adrift in near-Earth polar orbit.

The dataset contains images of Envisat, in both visible and LWIR modalities, arranged in sequences that simulate certain scenarios that might be faced by a chaser spacecraft as it approaches. The dataset

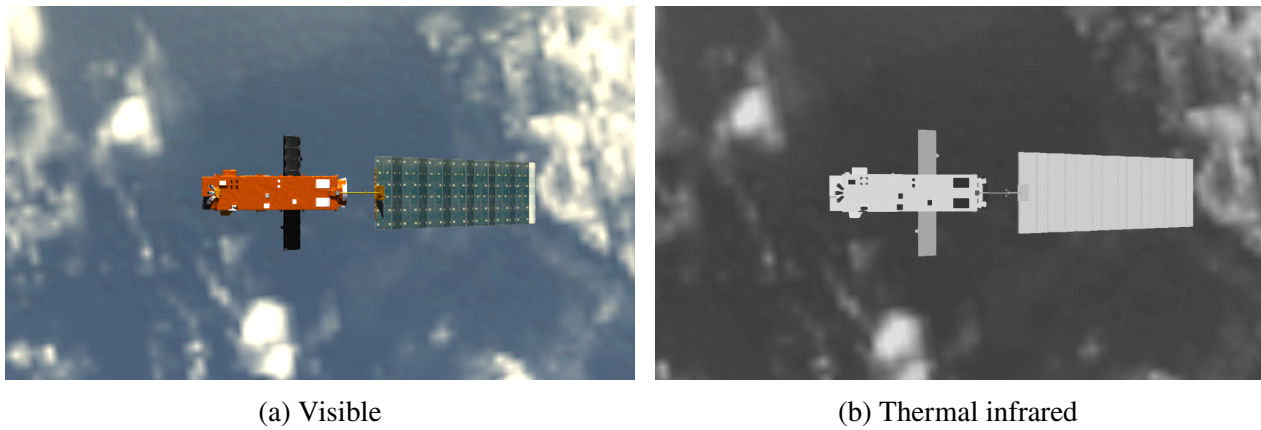


Fig. 2: Example images from the R-bar approach in the Astos Dataset featuring the Envisat spacecraft.

has been previously used to assess classical feature detection and description algorithms in the context of space rendezvous; see Rondao *et al.* [13] for details on the data generation for both modalities.

For the present study, we consider a dataset formed through a 50 %–50 % sampling from two simulated trajectories: 1) a negative V-bar approach vector such that the target is imaged against a black, deep space background; and 2) a negative R-bar approach, such that the target is imaged against the earth. In both cases, the chaser is at a hold point at 50 m relative distance, and the target is spinning about a single axis. Figure 2a shows an example of one such image from the R-bar sampling with the earth in the background, whereas Fig. 2b shows the same image in the LWIR.

Initially, a test was devised to train modified versions of Resnet18 and Resnet34 to be able to classify facets of the target into 10 classes, which each represent 36 deg of rotation along the azimuth. The network was trained purely on visible images, with each class containing 408. This included an even split of images taken from the R-bar and V-bar approach, and an even split of images showing the target in direct sunlight and an eclipse. A subset of 20 % of the training set was set aside as a validation set which could be used to stop training early to avoid over fitting. The test set contained the thermal counterparts of the visible images in the training set.

Both the visible and the thermal images are stored in .PNG format; as such, both have three colour channels in their current state. Whereas in the visible each channel represents the response in the red, green, and blue wavelengths separately, the thermal infrared represents a linear combination of the radiance for three sample wavelengths within the LWIR and the sensitivity of the simulated camera into a single image, and therefore the colour channels are all equal.

2.4 Jason-1 Dataset

Our chosen target for the second phase was Jason-1, another decommissioned oceanography satellite, which is currently in low Earth orbit around the equator. Jason-1 was a joint venture between National Aeronautics and Space Administration, USA (NASA) and Centre National d’Études Spatiales, France (CNES), and was originally launched in December 2001. In early 2012, Jason-1 was retired and placed into a graveyard orbit and contact was lost in June of that year. The satellite is not expected to re-enter Earth’s atmosphere for at least 1000 years; for this reason, as well as its in-operation, it is a prime candidate for an ADR mission [14].

Utilising a free to use Computer-Aided Design (CAD) model of Jason-1 as a basis, a laboratory mock-up was created, with a 1:4 scale replica with 1-DOF in rotation. Figure 3 shows images collected of

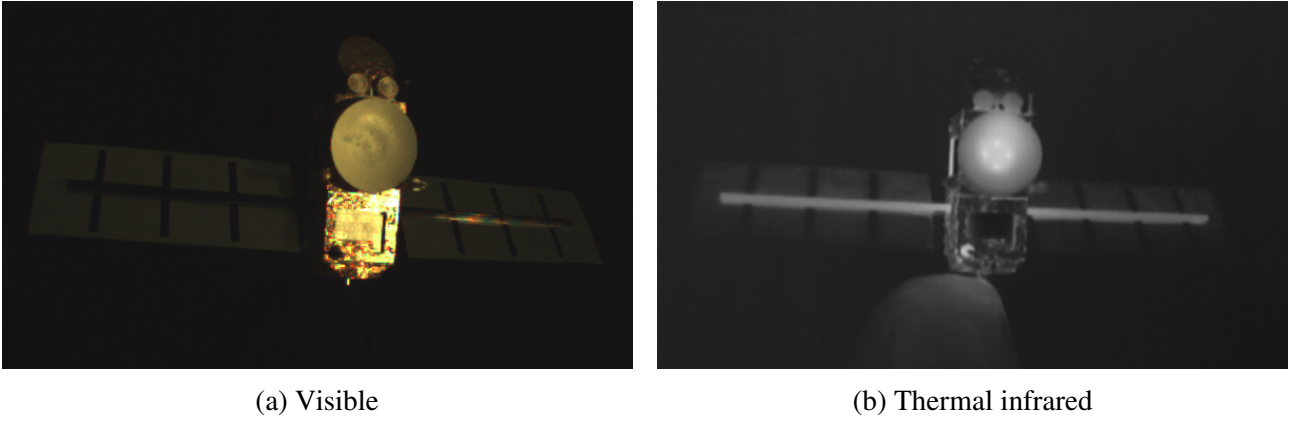


Fig. 3: Example images from the Jason-1 Dataset.

the mock-up in the lab in the visible and thermal infrared modalities. Whilst we tried to make our replica as faithful as possible to the real counterpart, some smaller components are not included since they would not be able to support themselves with their new scale, and other components needed to be reinforced such as the radiometer and the solar panels.

We did not have access to information on the thermal signature of Jason-1 in order to choose the materials for our replica. Therefore, we had to postulate from the data we had on Envisat (see Rondao *et al.* [13] and Yilmaz [15] for details) and heated the mock-up manually to achieve a similar signature. Both crafts share many of the same components (e.g., insulating foil, radiators); however, the attained thermal signature on Jason-1 is only an approximation since in reality they share different orbits and hence different Sun exposure patterns.

For training, we used the mechanical CAD model of the replica to generate synthetic visible images using the free and open source Blender modelling software.² The solar arrays of the CAD model were textured with real images from the target, whereas the foil was procedurally generated. Using the viewsphere sampling method outlined before (see Sec. 2.1), we generated all the possible facets of the 3D target at steps of 10 deg. Since we were working in two DOFs, we generated the facets across the entire 360 deg of azimuth and 180 deg of elevation, covering the complete viewsphere. Additionally, we created 21 copies of each image with different combinations of lighting conditions to create reflections and shadows on the body.

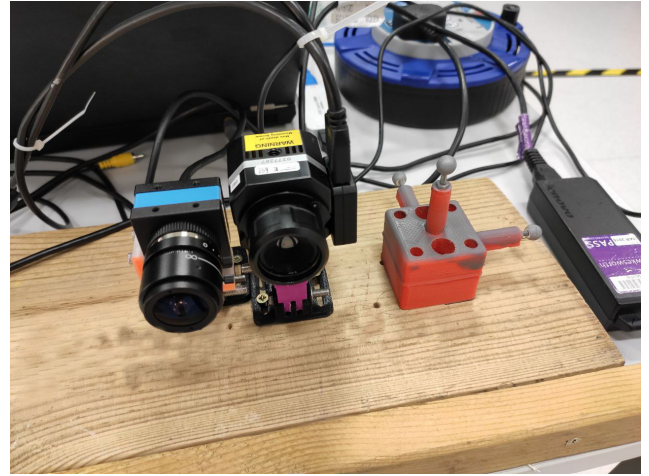
As stated before, our network uses two fully connected layers in parallel, one to produce a class for azimuth, and one to predict a class for elevation. Therefore, images belonging to any one of the 36 azimuth classes could belong to the same class for elevation, and conversely an image belonging to a single azimuth class could belong to any of the 18 classes representing elevation. Considering we have 21 copies of each image, this means that each class of azimuth had 378 training images, and each class of elevation had 756 training images.

For testing, we acquired a continuous sequence of images according to the laboratory setup in the next section. The replica Jason-1 rotates at 6 deg per second, and we captured two full rotations. Our cameras were acquiring at 10 Hz, which would give us around 1200 images, in reality we captured 1174 images for the test set.

²<https://www.blender.org>.



(a) Equipment layout



(b) Multimodal camera configuration

Fig. 4: ASL setup at City, University of London, for the acquisition of real images.

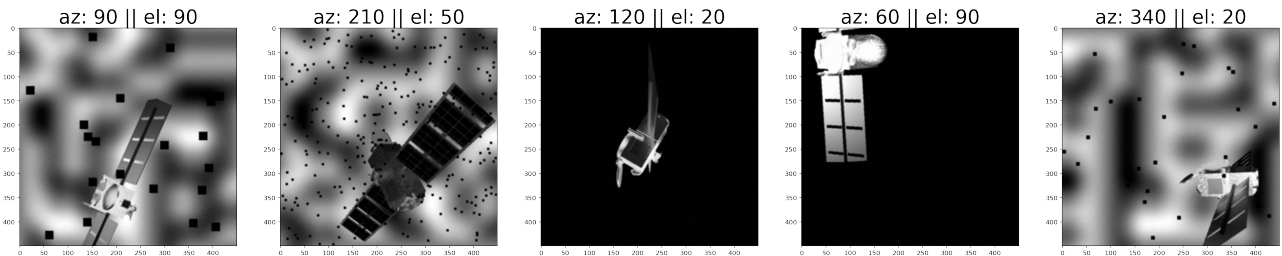


Fig. 5: Montage of images exemplifying some of the transformations introduced by our data augmentation pipeline.

2.5 Laboratory Setup

Data was collected in the Autonomous Systems Laboratory (ASL) at City, University of London. An image of the target mock-up within our laboratory setup can be seen in Fig. 4a. A blackout curtain was placed behind the target to simulate a deep space background. A floodlight was used to illuminate the target.

The facility is equipped with an OptiTrack motion tracking system that can record the 6-DOF of a target by detecting, tracking and triangulating markers that are placed in the target. The OptiTrack system was used to track the rotation of the target to provide the ground truth. We captured the target rotating around its vertical axis at a fixed distance of 1 m.

Our camera setup can be seen in Fig. 4b, with which both visible and thermal infrared images were captured simultaneously. This allowed us to compare the performance of our network on the real visible and real LWIR. The cameras are mounted side to side with a very small baseline to minimise the discrepancy between the images.

2.6 Augmentation Techniques

Image augmentation is a powerful tool which can be used to generate more data for which the network can learn from. However, it must be representative of the data that the developer is intending to encounter in the real-world when deploying the model. Carelessness could result in unwanted biases introduced into the dataset. In the first phase, we used augmentations including colour augmentation

Table 1: Performance metrics of our Resnet18 and Resnet34 architectures on the Envisat test set composed of synthetic thermal infrared images.

Architecture	Precision	Recall	F1 Score
Resnet18	0.819	0.839	0.819
Resnet34	0.883	0.896	0.883

to randomly change the brightness and hue before converting to greyscale. This would create new images of Envisat with different shades which would mimic what we may expect from thermal images.

We also applied positional and scale augmentations to randomly shift the image around the frame and scale up or down the image. When we moved to the second stage, we increased the magnitude of the translation and scale augmentations in order to make the network more robust to the variance of the target’s location within the frame. We took advantage of a technique presented by Proença and Gao [4] which used homography augmentations to warp the image in such a way to simulate variance in the camera rotation and roll.

We are concerned about our network’s robustness to variance in the thermal signature. As such, we wanted to prevent the network from becoming too dependent on certain shades of different components. The thermal signature could change depending on the time that the target had been in direct sunlight and for how long. Therefore, when we moved into the second stage of development we began to train on the red and blue channels of the synthetic images and validate on the green channel. Moreover, we randomly augmented the gain and contrast of the training set.

Our images were generated with an alpha channel so that we could easily mask the target and modify the background prior to it being loaded into the model. In order to simulate a diverse background, Perlin noise was generated and inserted into the background via the alpha channel. Perlin noise is typically employed by visual effects artists to increase the appearance of realism in computer graphics. In addition, we introduced additive Gaussian noise across the image to simulate sensor noise, and employed Gaussian blur so that features would appear softer, similar to what may be seen in thermal images.

Like Proença and Gao [4], we also employed patch dropout to randomly remove super pixels from the image, thus occluding certain features. This would encourage the network to rely on a more diverse group of features in order to make its predictions, making it more robust to differences between the computer model and the replica. Figure 5 shows examples images after our augmentations had been applied.

3 RESULTS

3.1 Evaluation on Synthetic Dataset

As stated before, in the first phase of development, we focused on proving the ResNet’s architecture suitability for our application. In order to do so we had to demonstrate that it was capable of classifying previously unseen LWIR facets of our target. For this purpose, the precision, recall, and F1 score metrics are used; these are commonly employed to gauge the performance of a classification algorithm. Precision can be calculated using Eq. (1), and is a measure of how many of the predictions allocated to a given class were in fact correct. Recall is calculated using Eq. (2); as can be seen this metric

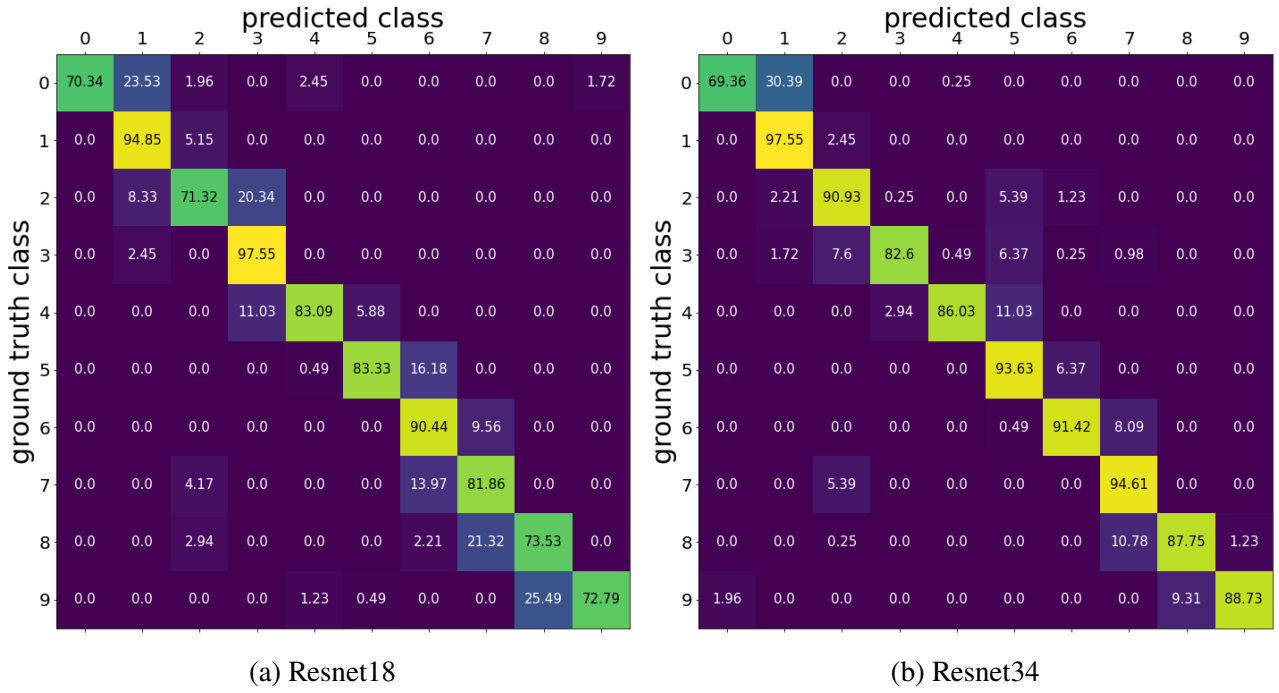


Fig. 6: Confusion matrices of results of our models on the Envisat test set composed of synthetic thermal infrared images.

accounts for false positives that occur in a given class.

$$\text{precision} = \frac{\text{true positives}}{\text{true positives} + \text{false positives}} \quad (1)$$

$$\text{recall} = \frac{\text{true positives}}{\text{true positives} + \text{false negatives}} \quad (2)$$

F1 score takes into account both precision and recall, and is calculated with Eq. (3). Given that false negatives and false positives are equally unwanted in our application, the F1 score will be an appropriate global metric to judge our network.

$$\text{F1}_{\text{score}} = 2 \times \frac{\text{precision} \times \text{recall}}{\text{precision} + \text{recall}} \quad (3)$$

During this investigation we trained two models based on Resnet18 and Resnet34 architectures. Table 1 shows the average precision, average recall, and average F1 score across all the classes. It can be seen that the deeper network did perform better on the test set in all three metrics.

These metrics do not measure the distance between the predicted class and the ground truth. In our application, a misclassification towards an adjacent class is not a major issue as it only represents a small rotation error. Hence, we also created the confusion matrices to look at where false predictions occurred; these can be observed in Fig. 6. One can see that the majority of false positives were misclassified as the adjacent class.

Both these results from Table 1 and Fig. 6 indicate that the networks we developed both performed well on the task presented to them. On the other hand, this represented a simpler problem as only one

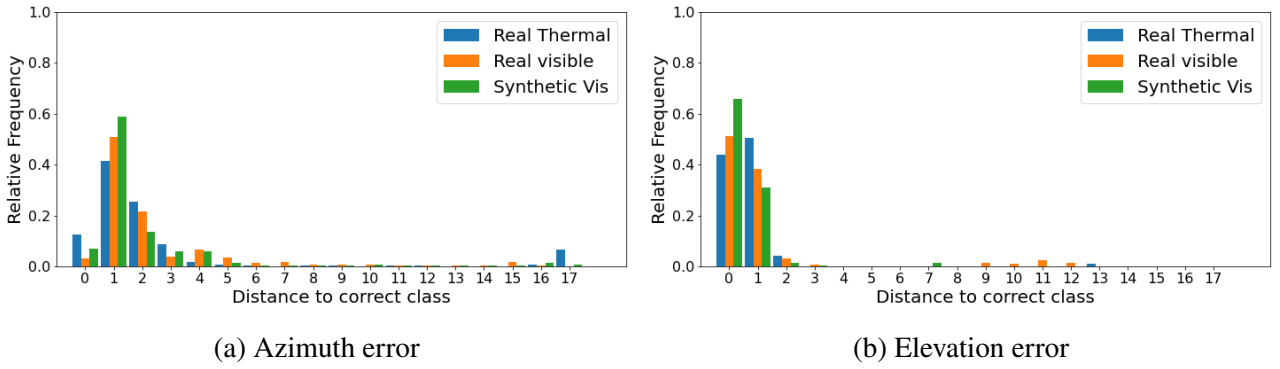


Fig. 7: Histogram of results on the Jason-1 real visible, real thermal infrared, and synthetic visible trajectory test sets.

Table 2: Absolute angular errors θ_{error} between the predicted viewpoint and the ground truth viewpoint.

Condition	Error (deg)	
	Mean	Median
Synthetic Visible	12.39	8.34
Real Visible	18.23	10.15
Real Thermal	19.27	10.75

DOF was considered. In addition, a relatively small number of classes (10) was considered, which meant that each one contained a relatively large set of viewpoints. This allows more leeway for the model’s predictions.

3.2 Evaluation on Real Dataset

As mentioned in Section 2.4, the Jason-1 training set was generated at discrete 10 deg steps in azimuth and elevation. However, the test set consists of a continuous trajectory which includes viewpoints in between those steps, thus evaluating the robustness of the model towards unseen perspectives. In addition to this, we created an additional test set by recreating this trajectory inside the Blender simulation environment by importing the ground truth recorded by Optitrack, along with the same lighting conditions. This provides a baseline test set which we could then use to compare the performance of our algorithm between synthetic and real data.

The orientation of the target in the test sets was grouped into bins of 10 deg in order to measure the distance between the predicted class and the ground truth class labels. Figure 7 shows the results for the performance on both the azimuth and elevation. Each colour represents a different condition: green for the synthetic visible test set; orange for the real visible test set; and finally blue for the real thermal infrared test set. For all three conditions, the majority of the predicted classes are found on the left-hand side of the two graphs, indicating that the network performed well on both DOFs.

The network performed better on the task of predicting the elevation — in all three conditions, over 90 % of the predictions were within a 1 bin distance, which is equivalent in a worst case scenario to an error of 20 deg. In the case of the azimuth, only 60 % of the synthetic set and 50 % of the real sets were within 1 bin. Nevertheless, we did find that around 80 % of the predictions for both real sets were within 2 bins, and thus within 30 deg (worst case scenario) from the ground truth.

We also calculated the absolute error between the predicted facet and the ground truth using Eq. (4).

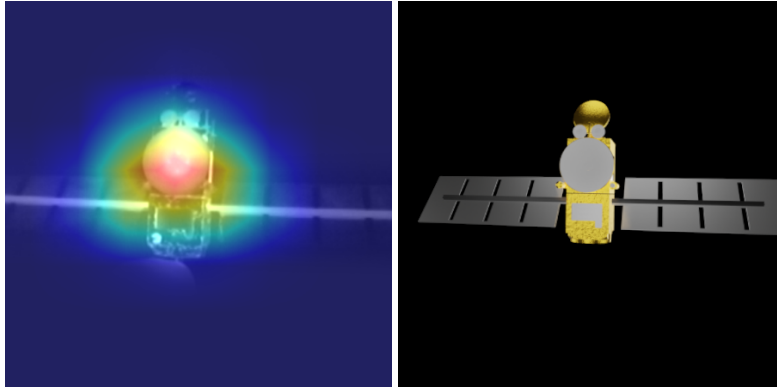


Fig. 8: Illustration of Grad-CAM for DNN-based spacecraft pose estimation explainability tested on the LWIR modality. The left figure shows the thermal infrared image which was fed to the network, overlaid with the Grad-CAM attention map generated by considering both the azimuth and elevation. The right figure shows the closest match according to the network.

To do so, we consider an imaginary line-of-sight vector drawn from the camera to the centre of the target. For the ground truth we denote this vector as V_{gt} ; similarly for the prediction we use V_{pr} . Since we are not considering the distance between the target and the chaser we can treat this as a unit vector. We can, therefore, take the inverse cosine of the dot product between the V_{gt} and V_{pr} to represent the principal angle error (disregarding the camera roll, since the viewpoint does not change with it):

$$\theta_{error} = \arccos(V_{gt} \cdot V_{pr}) \quad (4)$$

Table 2 shows the mean and median θ_{error} measured across the entire trajectory. It shows that for all three conditions the average error was less than 20 deg. We also found that the average error for both the lab datasets were close. It can be seen that approximately 10% of the predictions on the real thermal images are located 180 deg away from the ground truth, as indicated by the spike on the right-hand side of the plot in Fig. 7. This would contribute significantly to the average absolute error. We speculate that the cause of this phenomenon is due to the symmetrical nature of our target.

3.3 Evaluation Using Grad-CAM

DNNs have achieved unprecedented performance in many applications, although they remain opaque tools. Simply inspecting the model’s structure, or analysing its weights, tells us very little about its decision-making behaviour. In addition, relying on simple metrics such as F1, recall and precision, can lead a developer to overestimate the capability of their models. In order to better understand the models developed on Jason-1, we have employed Grad-CAM to identify the sections of the target that the model relied on to make predictions.

This could be done in different ways, either by encoding both predictions for azimuth and elevation, or we could treat them as mutually exclusive, and investigate one or the other. Initially we were interested in investigating where the network’s focus was considering both, since this will give us a general sense of how it made decisions. This is done in much the same way as outlined by Selvaraju *et al.* [10], except since we have two outputs, each is one-hot encoded, and then summed together prior to backpropagation.

We discovered that, throughout the trajectory, the network’s attention was focused heavily on the central bus; an example is shown in Fig. 8. This is logical since it is both the centre of the target and

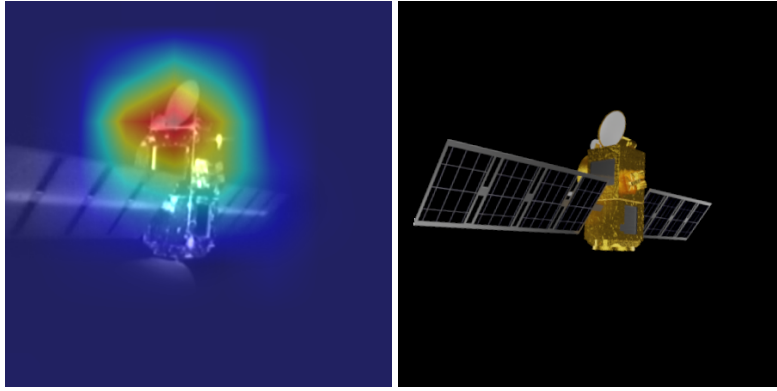


Fig. 9: Illustration of a good match between the ground truth (left) and the prediction (right). The Grad-CAM was applied only taking into account the azimuth class.



Fig. 10: Illustration of a bad match between the ground truth (left) and the prediction (right). The Grad-CAM was applied only taking into account the azimuth class.

also where many of its unique components are found, such as the radiators and instrument antennas. These are the components which would be absent if we were looking at the target from a vastly different orientation.

We were also interested in what caused the network to misclassify the azimuth of some thermal infrared images 180 deg away from the ground truth. Therefore, we applied Grad-CAM again, but this time only using the one-hot encoding of the azimuth class, and while completely ignoring the elevation prediction. Figure 9 shows an example where this method is applied to a correctly predicted orientation. We can see that the focus is on the bus, but particularly concentrated at the top near what would be the radiometer.

Juxtaposed, Fig. 10 shows the next frame which occurs in one of the instances where the model misclassified the target 180 deg out. We can see in this image the model's focus has shifted away from the central bus to include the solar panels. This supports our speculation, stated in the previous section, that the symmetrical nature of the target caused the network to make the misclassification, since the solar panels are symmetrical. This is made more difficult in the thermal infrared, since the patterns on the front of the panels cannot be made out. Moreover, the supports for the panels radiated heat slower, and could be seen through the panels.

We investigated further by repeating this procedure on the real visible images we had collected. Figure 11 shows a frame from the visible camera that was captured at the same time as the offending frame shown in Fig. 10 was captured. We found that, when viewing facets on this side of the target such as the one shown, much of the attention was on the surface of the solar panels. This indicates

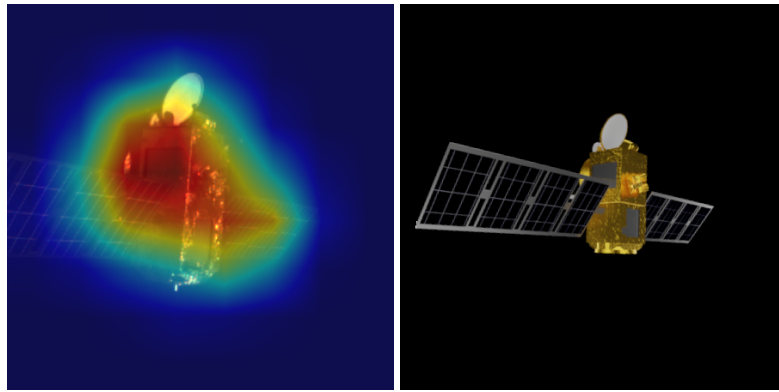


Fig. 11: Illustration of Grad-CAM for DNN-based spacecraft pose estimation explainability tested on the visible modality. The left image shows the visible image which was fed to the network, overlaid with the Grad-CAM attention map which was generated this only considering the azimuth. The right image shows the closest match according to the network.

that the model is biased to search for this pattern, and the fact that it is absent from the thermal images put the network at a disadvantage.

4 CONCLUSION

Our goal in this study was to develop a CNN to predict the coarse viewpoint of a target as imaged by a rendezvousing chaser for the initialisation of spacecraft relative pose estimation algorithms, and to evaluate its robustness on thermal infrared imagery when it has been trained exclusively on visible images. During our investigation, we firstly demonstrated this capability on a synthetic dataset of the spacecraft Envisat. We then expanded our investigation to real images of the Jason-1 spacecraft captured in our laboratory. In this phase we demonstrated our network could perform just as well on real thermal infrared images as it could on real visible images.

Our experimental set up is currently limited to only one degree of rotation and does not allow us to test all possible permutations of azimuths and elevations. Therefore, we cannot verify our model's performance on all possible orientations of a real target, which will need to be proven in order for our model to be deployed in the wild. Nevertheless, for the available facets of our real target, we have demonstrated our network is able to achieve an average accuracy greater than 20 deg in both modalities.

Moreover, we have gone a step further by attempting to explain how our network makes decisions. From our investigations with Grad-CAM we were able to better understand that the features on the central bus were key to the network's performance. Furthermore, we were able to better understand its failure modes, which we identified as the textures on the solar panels. This weakness can be removed from the CAD model in future work to achieve better performance in later iterations.

As mentioned, the focus of our network tended towards the central bus of the target, therefore future work will examine how well the Grad-CAM maps match the target's location within the frame. From our observations in this study, we expect this can be used to explicitly predict a coarse position of the target. In addition, we will also investigate the performance of our network in other conditions which might occur on orbit such as in eclipse. This will allow us to evaluate in conditions where we'd expect thermal images to provide better clarity of the target than visible.

REFERENCES

- [1] Fricke, R. W., *STS-49: Space shuttle mission report*, Provided by the SAO/NASA Astrophysics Data System, Jul. 1992. [Online]. Available: <https://ui.adsabs.harvard.edu/abs/1992sts..reptQ....F>.
- [2] Opromolla, R., Fasano, G., Rufino, G. and Grassi, M., ‘A review of cooperative and uncooperative spacecraft pose determination techniques for close-proximity operations,’ *Progress in Aerospace Sciences*, vol. 93, pp. 53–72, 2017, ISSN: 0376-0421. DOI: <https://doi.org/10.1016/j.paerosci.2017.07.001>.
- [3] Sharma, S. and D’Amico, S., *Pose estimation for non-cooperative rendezvous using neural networks*, 2019. arXiv: [1906.09868](https://arxiv.org/abs/1906.09868) [cs.CV].
- [4] Proença, P. F. and Gao, Y., *Deep learning for spacecraft pose estimation from photorealistic rendering*, 2019. arXiv: [1907.04298](https://arxiv.org/abs/1907.04298) [cs.CV].
- [5] Rondao, D., Aouf, N., Richardson, M. A. and Dubanchet, V., ‘Robust on-manifold optimization for uncooperative space relative navigation with a single camera,’ *Journal of Guidance, Control, and Dynamics*, vol. 44, no. 6, pp. 1157–1182, 2021. DOI: [10.2514/1.G004794](https://doi.org/10.2514/1.G004794).
- [6] Hajebi, K. and Zelek, J. S., ‘Structure from infrared stereo images,’ in *2008 Canadian Conference on Computer and Robot Vision*, 2008, pp. 105–112. DOI: [10.1109/CRV.2008.9](https://doi.org/10.1109/CRV.2008.9).
- [7] Yılmaz, Ö., Aouf, N., Majewski, L., Sanchez-Gestido, M. and Ortega, G., ‘Using Infrared Based Relative Navigation for Active Debris Removal,’ in *10th International ESA Conference on Guidance, Navigation and Control Systems*, Salzburg, Austria: ESA, 2017, pp. 1–16.
- [8] He, K., Zhang, X., Ren, S. and Sun, J., ‘Deep Residual Learning for Image Recognition,’ in *2016 IEEE Conference on Computer Vision and Pattern Recognition (CVPR)*, IEEE, Jun. 2016. DOI: [10.1109/cvpr.2016.90](https://doi.org/10.1109/cvpr.2016.90).
- [9] He, L., Aouf, N. and Song, B., *Explainable deep reinforcement learning for uav autonomous navigation*, 2021. arXiv: [2009.14551](https://arxiv.org/abs/2009.14551) [cs.R0].
- [10] Selvaraju, R. R., Cogswell, M., Das, A. *et al.*, ‘Grad-cam: Visual explanations from deep networks via gradient-based localization,’ *International Journal of Computer Vision*, vol. 128, no. 2, pp. 336–359, Oct. 2019, ISSN: 1573-1405. DOI: [10.1007/s11263-019-01228-7](https://doi.org/10.1007/s11263-019-01228-7).
- [11] LeCun, Y., Jackel, L., Boser, B. *et al.*, ‘Handwritten Digit Recognition: Applications of Neural Network Chips and Automatic Learning,’ *IEEE Communications Magazine*, vol. 27, no. 11, pp. 41–46, Nov. 1989. DOI: [10.1109/35.41400](https://doi.org/10.1109/35.41400).
- [12] Jocher, G., Stoken, A., Borovec, J. *et al.*, *Ultralytics/YOLOv5*, version v5.0, Apr. 2021. DOI: [10.5281/zenodo.4679653](https://doi.org/10.5281/zenodo.4679653).
- [13] Rondao, D., Aouf, N., Richardson, M. A. and Dubois-Matra, O., ‘Benchmarking of local feature detectors and descriptors for multispectral relative navigation in space,’ *Acta Astronautica*, vol. 172, pp. 100–122, 2020, ISSN: 0094-5765. DOI: <https://doi.org/10.1016/j.actaastro.2020.03.049>.
- [14] *Long-Running Jason-1 Ocean Satellite Takes Final Bow*, 2013. [Online]. Available: <https://www.jpl.nasa.gov/news/long-running-jason-1-ocean-satellite-takes-final-bow> (visited on 20/05/2021).
- [15] Yılmaz, Ö., ‘Infrared Based Monocular Relative Navigation for Active Debris Removal,’ Ph.D. dissertation, Cranfield University, Shrivenham, United Kingdom, 2018.